ACS OMEGA

Open Access

http://pubs.acs.org/journal/acsodf

Article

Heterogeneous Models for UV Induced Precursor-Mediated Growth of CdS Nanoparticles in PMMA Films: Fitting Experimental Curves and Core−Shell Growth

Nikita Bityurin,* Natalia Sapogova, Andrey Kudryashov, and Alexander Pikulin

Cite This: *ACS Omega* 2024, 9, 36648−36658

Read Online

ACCESS | Metrics & More | Article Recommendations

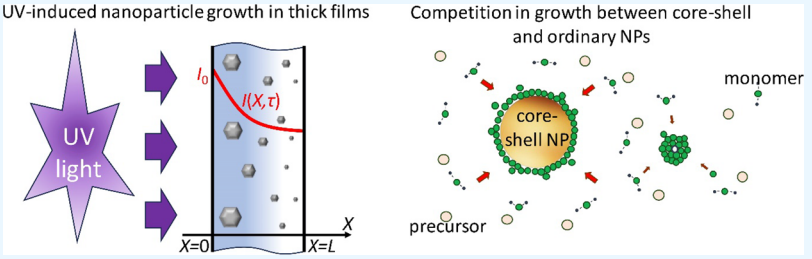

ABSTRACT: Experimental data on the absorbance evolution of an UV irradiated PMMA film containing the TEDBCd CdS precursor published earlier are fitted by the authors' recently published model of precursor-mediated heterogeneous nucleation and growth of nanoparticles in polymer films. Two types of nucleation centers are considered. The centers of the first type are nanoparticles initially existing in the material. The centers of the second type belong to polymer chains. The study shows that the experimental data indicate a wide size distribution of the obtained CdS nanoparticles. For the estimated parameter values, the problem of core−shell nanoparticle growth where the nucleation centers of the first type are nanoparticles of a different nature is considered.

1. INTRODUCTION

Photoinduced nanocomposites are initially homogeneous materials in which inorganic nanoparticles are formed under the effect of UV/laser radiation.[1−22] In the following, we consider photoinduced nanocomposites consisting of a polymer matrix with dissimilated precursor molecules. The polymer matrix with precursor can be prepared either by casting or polymerization.[1,18,22] Light-induced decomposition of these molecules leads to the nucleation and growth of nanoparticles. The resulting nanoparticles can be metal, which gives the nanocomposite plasmonic properties.[1,5,9,11] Alternatively, they can be of semiconductor nature, which imparts the properties of semiconductor nanoparticles, such as particular characteristic luminescence spectra, to the materials produced.[2−4,6−8,10,12−22] The idea of obtaining nanoparticles of a different nature in the same sample opens up new promising opportunities.[23,24] The advantage of photoinduced nanocomposites is that different kinds of structures with different optical properties can be recorded within the initially transparent media either by direct laser writing[3] or by using masks.[25] This makes photoinduced nanocomposites promising for photonic applications.[3]

This paper considers the evolution of absorbance at the probing wavelength in the case of precursor-mediated UV induced heterogeneous nucleation and growth of CdS nanoparticles in PMMA films. We will fit the experimental data published in.[20] In that work, PMMA films with a thickness of about 200 μm were prepared by casting from toluene solution. The films contained a 5% mass fraction of the well-soluble precursor bis(1,1,5,5-tetraethyl-2,4-dithiobiureto)-cadmium(II)[$Cd(N(SCNEt_2)_2)_2$] (TEDBCd) proposed earlier.[26,27] The obtained films were of good quality and transparent in the optical range. The films were irradiated by a light-emitting diode (LED) operating at a wavelength of 365 nm at different intensities and different temperatures. The irradiation resulted in the appearance of increasing optical absorption in the optical range. The transmission electron microscopy (HR TEM) data allowed one to relate this absorption increase with the nucleation and growth of CdS nanoparticles. In situ monitoring of the process was performed at a wavelength of 405 nm, at which the samples are initially transparent.

Received: May 31, 2024
Revised: July 30, 2024
Accepted: August 9, 2024
Published: August 19, 2024

Theoretical models have been developed taking into account photochemically induced precursor-mediated nanoparticle nucleation and growth in polymer films. The papers consider either homogeneous[28] or heterogeneous[29] nucleation of nanoparticles.

These theories belong to a broader class of models that consider the photochemical modification of a material under the effect of monochromatic UV irradiation. UV photons are absorbed by certain species present in the material, thereby initiating processes that lead to its modification. There is an important class of such processes for which the final result of photon-induced transformations is determined by the irradiation exposure, the integral of the light intensity over time. When the light intensity is constant, the exposure is equal to the product of the intensity and the irradiation time. A process belonging to this class can be tested by irradiating the material at different intensities such that the product of intensity and irradiation time remains constant.[30−33] If the irradiation result is the same for different attempts, this means that the exposure determines the material alteration, not the intensity or irradiation time individually. The kinetics of the process can be monitored using either a probing monochromatic beam[20] or white light from a lamp[30,32] or LED.[34]

In the case of optically thin samples, the absorption is relatively small, and it can be assumed that the intensity of the incident UV radiation is the same throughout the film.[28,29] In optically thick films, the outer layers shield the inner layers, and the light intensity in the inner layers differs from the input intensity. The material alteration leads to a change in the optical properties, including the absorption spectra. Thus, the absorption coefficient at the irradiation wavelength changes during the process.

This means that even if the irradiation intensity is constant in time, the intensity in the inner layers of optically thick films is time dependent. This creates certain difficulties for the development of an analytical model of the kinetics of material change in thick films. However, in refs 35−37, a mathematical approach that solves this problem has been developed.

Importantly, the published experimental data[20] on UV irradiation of precursor-containing polymer films show the dependence of absorbance at the probing wavelength on the UV irradiation exposure. Theoretical consideration suggests that under some conditions UV induced nucleation and growth of nanoparticles in polymer films can be described by a heterogeneous model. This model permits one, contrary to the homogeneous case, to explain the dependence of the process parameters, including absorbance, on UV exposure.

Core−shell nanoparticles have improved optical and other properties.[38−45] It is of great interest to obtain them directly in a solid matrix. The next application of the theory of precursor-mediated heterogeneous growth of nanoparticles considered in the present work is the model of shell growth on existing core nanoparticles within the matrix. In contrast to the model considered in ref 23, where shell growth is initiated by laser heating of the metal core directly near the nanoparticle, the present work reveals a precipitation mechanism (see, e.g., ref 39) initiated by homogeneous decomposition of the precursor compound.

The paper is organized as follows.

In the Methods section, we review two theoretical approaches that are used in this work. The first one is the calculation of the absorbance evolution in the problem of photochemical alteration of thick films. It is described in Section 2.1. In Section 2.2, we review the main results obtained using the heterogeneous model of nucleation and growth of nanoparticles in polymer films[29] and write down the basic formulas needed in what follows.

The results and discussion consist of three parts. In the first part, presented in Section 3.1, the approach discussed in Section 2.1 is applied to the model described in Section 2.2. The second part, presented in Section 3.2, involves fitting experimental curves from[20] using the formulas obtained in Section 3.1.

In Section 3.3, based on the parameter values determined in Section 3.2, some features of the problem of photochemically induced growth of core−shell nanoparticles when core nanoparticles are initially present in the polymer sample are elucidated. The competition between the shell growth and the growth of pure native nanoparticles is considered.

2. METHODS

In this section, we consider two theoretical models that are used to understand and fit experimental data.

2.1. Model of Absorption Evolution due to Photochemical Material Alteration in Thick Films. Consider a flat homogeneous film of thickness L with a boundary located at the point $X = 0$, where X is a coordinate. The film is irradiated by UV light normally incident on the surface with intensity I_0 (see Figure 1). In general, I_0 can be time-dependent. Irradiation leads to numerous processes, which may involve many $\{S_i\}$ species with different properties (see, e.g., the corresponding equations in refs 30−32). Below we consider the heterogeneous nucleation and growth of inorganic, semiconductor nanoparticles within polymer films where the nanoparticles of each size should be considered as separate species with their unique optical properties. Here, the number of different species is close to infinity. Nevertheless, if the net process is exposure-dependent, the set of kinetic equations can be reduced to the following (see refs 35 and 36):

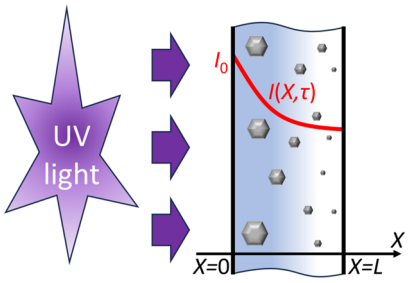

Figure 1. Schematic representation of the thick-film problem. The film is irradiated by UV light with intensity I_0. The light absorption in the film is nonuniform along the X coordinate and varies in time due to the UV induced particle growth.

$$\frac{\partial s}{\partial \tau} = \Psi(s)q \tag{1}$$

$$\frac{\partial q}{\partial x} = -\alpha(s)q \tag{2}$$

$$\frac{\partial q_p}{\partial x} = -\alpha_p(s)q_p \tag{3}$$

$$s(x, t = 0) = s_{init} \tag{4}$$

https://doi.org/10.1021/acsomega.4c05121
ACS Omega 2024, 9, 36648−36658

$$q(x = 0, t) = 1 \tag{5}$$

$$q_p(x = 0, t) = 1 \tag{6}$$

here, x is a dimensionless coordinate, which is usually normalized to the initial penetration depth of UV light, τ is a dimensionless variable playing the role of time, which is an explicit increasing function of exposure $\tau \propto \int_0^t I_0\,dt$, q is a dimensionless intensity $q(x,\tau) = I(x,\tau)/I_0(\tau)$, and $s(x,\tau)$ is a dimensionless variable fully characterizing the degree of alteration of the material at point x at "time" τ. The correct choice of this variable is very important.

It is productive to in situ monitor the process using probing radiation. In ref 20, the probing wavelength is in the transparency region of the original sample. In principle, this can be done by measuring the optical spectrum with a white LED or a special lamp.[30,34] In eq 3 we consider one more variable, namely q_p, which is the dimensionless intensity of the probing light at some frequency ω_p, and α and α_p are the corresponding dimensionless absorption coefficients at the irradiation wavelength and at the probing wavelength.

The experiment usually monitors the transmittance at the probing wavelengths or, more precisely, the absorbance. Speaking about absorbance D, it is understood that $\exp(-D) = I(X = L)/I(X = 0)$ or, with variables of eqs 1−6,

$$q(x = l) = \exp(-D) \tag{7}$$

here, l is the dimensionless quantity L. The expression for D is obtained in ref 37. There, the expression for the absorbance D_p at the probing wavelength is presented as a function of dimensionless time, which is proportional to the exposure. It is written as a function of the value of the variable s at $x = 0$, here $s^0 \equiv s(x = 0)$:

$$D_p(s^0) = \int_0^l \alpha_p(s(x, s^0))dx = \int_{s^l(s^0)}^{s^0} \frac{\alpha_p(s)ds}{\Psi(s)\int_{s_{init}}^{s}\frac{\alpha(s')}{\Psi(s')}ds'} \tag{8}$$

and at the irradiation wavelength

$$D(s^0) = \int_0^l \alpha(s(x, s^0))dx = \ln\frac{\int_{s_{init}}^{s^0}\frac{\alpha(s')}{\Psi(s')}ds'}{\int_{s_{init}}^{s^l(s^0)}\frac{\alpha(s')}{\Psi(s')}ds'} \tag{9}$$

here,

$$s^l \equiv s(x = l) \tag{10}$$

s^0 as a function of τ (which is proportional to the exposure) can be found from eqs 1, 4, and 5, and $s^l(s^0)$ can be found from the ordinary differential equation

$$\frac{ds}{dx} = \Psi(s)\int_s^{s_{init}}\frac{\alpha(s')}{\Psi(s')}ds' \tag{11}$$

with boundary condition

$$s(x = 0) = s^0 \tag{12}$$

2.2. Evolution of the Particle Size Distribution in the Problem of Precursor-Mediated Nanoparticle Nucleation and Growth: Analytical Solutions. A model of heterogeneous precursor-mediated nucleation and growth of inorganic nanoparticles in polymer films was formulated in ref 29. Below we address a few equations and formulas that will be needed in what follows. A polymer film contains a precursor compound with number density A, which decomposes photochemically to release a "monomer" B; B_n is a number density of the nanoparticles containing n monomers. Nanoparticle growth occurs when monomers are added. The initial value of A is A_0. The precursor decomposes according to the equation

$$\frac{\partial A}{\partial t} = -\sigma_A\eta_A AI \tag{13}$$

where I is the light intensity measured in photon/cm^2 s, σ_A is the absorption cross section, and η_A is the quantum yield of precursor decomposition.

We introduce a variable $C = \sum_{n=1}^{\infty} nB_n$, which is the monomer number density inside all the nanoparticles.[29] There is an approximate equality

$$A + C = A_0 \tag{14}$$

By introducing dimensionless variables $b_n = B_n/A_0$ and passing from the discrete variable n to the continuous variable z, the size distribution of the nanoparticles can be obtained as $b(z)$. For the dimensionless variant $c = C/A_0$, we have

$$c = \int_0^{\infty} b(z)zdz \tag{15}$$

It was shown in ref 29 that along with physical variables (b, z) it is useful to consider artificial variables (g, ξ),

$$g(z) = k(z)b(z) \tag{16}$$

$$k(z) = 1 + z^{1/3} \tag{17}$$

$$\xi(z) = \int_0^z \frac{dz}{k(z)} = -3z^{1/3} + 3\cdot\ln(1 + z^{1/3}) + \frac{3}{2}z^{2/3} \tag{18}$$

In variables (g, ξ), the kinetic equation considering the evolution of the nanoparticle size distribution is given by (see eq 26 in ref 29)

$$\frac{\partial g}{\partial c}\frac{1}{V(c)} + \frac{\partial g}{\partial \xi} = 0 \tag{19}$$

It was mentioned in ref 29 that its solution is generally a nondeformable profile propagating along the ξ axes with velocity $V(c) = \int_0^{\infty} g(z)dz$:

$$g(\xi, c) = g(\xi - \int_0^c V(c')dc') \tag{20}$$

The shape of this profile can be found from the initial and boundary conditions.

Following,[29] we consider two different cases of heterogeneous nucleation. In the first one, further referred to as Model I, the nucleation centers are actually nanoparticles formed during the film preparation. Here, part of the precursor compound initially is destroyed and $A(t = 0) < A_0$. Thus, eq 19 should be supplemented with an initial condition for the nanoparticle size distribution. Due to the requirement that the nanoparticles are immobile, some minimum nanoparticle size must be present in the system to fulfill this condition. In refs 28 and 29, it was estimated that for CdS nanoparticles in PMMA matrix at temperatures near the glass transition point, the

https://doi.org/10.1021/acsomega.4c05121
ACS Omega 2024, 9, 36648−36658

mobility of the nanoparticles with $n \geq 70$ is almost zero. Thus, the initial size distribution starts from $n \geq 70$.

To be specific, we consider the simplest solution of the problem, following.[29] If the initial distribution of g on the ξ axis is

$$g = g_0 \text{ at } \xi_{R0} < \xi < \xi_{F0} \text{ and } g = 0 \text{ at } \xi < \xi_{R0} \text{ or } \xi > \xi_{F0} \tag{21}$$

where $\xi_{R0,\,F0}$ are the initial positions of the rear and leading fronts of the distribution, then as the leading front ξ_F shifts to the value

$$\xi_F = \xi_{F0} + \delta\xi \tag{22}$$

the distribution comes to

$$g = g_0 \text{ at } \xi_R < \xi < \xi_F \text{ and } g = 0 \text{ at } \xi < \xi_R \text{ or } \xi > \xi_F \tag{23}$$

where

$$\xi_R = \xi_{R0} + \delta\xi \tag{24}$$

In physical variables (b, z), this solution reads

$$b(z, z_F) = \frac{g_0}{1 + z^{1/3}} \text{ at } z_R \leq z \leq z_F \text{ and } b(z, z_F) = 0 \text{ at } z < z_R \text{ or } z > z_F \tag{25}$$

here, g_0 is a constant factor. In order to find solution, we fix z_F and find z_R, using the equation

$$\xi(z_R) = \xi(z_F) - \xi(z_{F0}) + \xi(z_{R0}) \tag{26}$$

The relation between ξ and z is determined by eq 18.

The evolution of the nanoparticle size distribution (25) is shown in Figure 3 of ref 29. The function c (see eq 15) can also be represented as a function of z_F.

$$c(z_F) = \int_{z_R(z_F)}^{z_F} \frac{g_0 z}{1 + z^{1/3}} dz = g_0 F(z_R(z_F), z_F) \tag{27}$$

where

$$F(z_1, z_2) = 3((z_2^{1/3} - z_1^{1/3}) - \frac{1}{2}(z_2^{2/3} - z_1^{2/3}) + (z_2 - z_1) - \frac{1}{4}(z_2^{4/3} - z_1^{4/3}) + \frac{1}{5}(z_2^{5/3} - z_1^{5/3}) - \ln(\frac{1 + z_2^{1/3}}{1 + z_1^{1/3}})) \tag{28}$$

Initially, $c = c_{init} > 0$,

$$c_{init} = g_0 F(z_{R0}, z_{F0}) \tag{29}$$

and

$$c(z_F) = c_{init} \frac{F(z_R(z_F), z_F)}{F(z_{R0}, z_{F0})} \tag{30}$$

One can find the exposure

$$E_{exp} = \hbar\omega_{irr} \int_0^t I dt' \tag{31}$$

which corresponds to a given value of c,

$$E_{exp}(z_F) = \frac{1}{\beta} \ln(\frac{1 - c_{init}}{1 - c(z_F)}),\ \beta = \eta_A \frac{\sigma_A}{\hbar\omega_{irr}} \tag{32}$$

here, $\hbar\omega_{irr}$ is the energy of the photon at the irradiation wavelength.

Thus, fixing z_F, one can find the nanoparticle size distribution (25), $c(z_F)$ (see eqs 28−30 and then $E_{exp}(z_F)$, see eq 32). This means that we have an exposure dependence of the size distribution in parametric form, where the parameter to be excluded is the front position z_F (or the size of the largest nanoparticle in the continuous approximation).

In the second case (hereafter referred to as Model II), the nucleation centers belong to the polymer matrix and are located on the polymer chains, which are almost immobile.

The monomer enters the primary nucleation center (the initial number density of centers is $\bar{B}_{00}$) and transforms into a nanoparticle B_1 with probability γ.

In variables (g, ξ), the solution of the problem is a nondeformable profile propagating from minus infinity in such a way that the shift $\delta\xi$ of this profile along the ξ axis corresponds to the position of the leading front,

$$\xi_F = \delta\xi \tag{33}$$

The solution suggests that at a given value of ξ_F and $\xi < \xi_F$

$$g(\xi, c) = \gamma \frac{\bar{B}_{00}}{A_0} \exp(\gamma(\xi - \xi_F(c))) \tag{34}$$

and $g(\xi, c) = 0$ for $\xi > \xi_F$. Coming back to physical variables, we have

$$b(z, z_F) = \gamma \frac{\bar{B}_{00}}{A_0} \frac{\exp(\gamma(\xi(z) - \xi(z_F)))}{1 + z^{1/3}} \tag{35}$$

and

$$c(z_F) = \gamma \frac{\bar{B}_{00}}{A_0} \exp(-\gamma\xi(z_F)) j(\gamma, z_F) \tag{36}$$

where

$$j(\gamma, z) = \int_0^z \exp(\gamma(\xi(z'))) \frac{z'}{1 + (z')^{1/3}} dz' \tag{37}$$

The examples of the evolution of the size distribution according to the solution 35) are shown in Figure 6 of ref 29. The dependence of the exposure on z_F follows from eq 32 at $c_{init} = 0$.

With known nanoparticle size distribution and dependence of the absorption cross section of a nanoparticle on its size, it is possible to calculate the absorption coefficient of the nanocomposite and its dependence on exposure. In a general form, this is discussed in ref 29.

The present consideration is aimed at fitting the experimental data[20] on the exposure dependence of optical absorbance of PMMA film with CdS precursor compounds. Thus, we consider the size dependence of the absorption cross section of CdS nanoparticles in PMMA using the approximation proposed in ref 37.

We consider the absorption of CdS nanoparticles at two wavelengths, namely, an irradiation wavelength of 365 nm and a probing wavelength of 405 nm. Both of these wavelengths are slightly shorter than the wavelength corresponding to the band gap in bulk CdS, 513 nm. This means that sufficiently small CdS nanoparticles are transparent at a wavelength of 365 nm due to quantum confinement. Absorption at this wavelength becomes significant for CdS nanoparticles larger than $z^* = 216$ (see ref 37 for details). According to the model considered in

https://doi.org/10.1021/acsomega.4c05121
ACS Omega 2024, 9, 36648−36658

refs 37 and 29, the absorption cross section of any nanoparticle of size $z > z^*$ is proportional to z. That is, the absorption cross section of a particle is σz, where σ is the absorption cross section per monomer included in the nanoparticle. Estimates made in ref 37 show that $\sigma = 5 \times 10^{-18}$ cm^2.

Similarly, this consideration can be applied to the absorption at the probing wavelength. Here, the nanoparticles with $z < z^{**}$ with $z^{**} = 340$ are transparent for probing light, and the absorption cross section of the nanoparticles with $z > z^{**}$ is $\sigma_p z$, where (see ref 37) $\sigma_p = 4.2 \times 10^{-18}$ cm^2.

In the following, we will operate with dimensionless absorption coefficients (see eqs 2 and 3), which are normalized to the initial absorption coefficient of the film at the irradiation wavelength $\sigma_A A_0$. The conditions of the discussed experiment are estimated[37] to be $A_0 = 6 \times 10^{19}$ cm^{-3} and $\sigma_A = 4 \times 10^{-19}$ cm^2. Let us introduce dimensionless cross sections

$$\sigma^* = \sigma/\sigma_A \text{ and } \sigma^{**} = \sigma_p/\sigma_A \tag{38}$$

and functions

$$f(z_F) = \int_{z^*}^{\infty} b(z, z_F) z dz \text{ and } f_p(z_F) = \int_{z^{**}}^{\infty} b(z, z_F) z dz \tag{39}$$

Taking into account the approximate relation 14, we finally obtain (see eqs 1−6)

$$\alpha(z_F) = 1 - c(z_F) + \sigma^* f(z_F) \tag{40}$$

$$\alpha_p(z_F) = \sigma^{**} f_p(z_F) \tag{41}$$

3. RESULTS AND DISCUSSION

3.1. Solution of the Problem of the Exposure Dependence of the Absorbance of Thick Films for Model I and Model II.

Relations 40 and 41 show that absorption coefficients at both irradiation and probing wavelengths are explicit functions of z_F, which is the maximum size of nanoparticles in the continuous approximation. Equation 14 after the introduction of dimensionless time (see eqs 31 and 32)

$$\tau = \beta E^0_{exp} \tag{42}$$

reads

$$\frac{\partial c}{\partial \tau} = (1 - c) q \tag{43}$$

The superscript in (42) means that the exposure is taken at $X = 0$. Keeping in mind that c is the explicit function of z_F (see eqs 32 and 30), one can write

$$\frac{\partial c}{\partial \tau} = \frac{dc}{dz_F}\frac{\partial z_F}{\partial \tau} \text{ or } \frac{\partial z_F}{\partial \tau} = \frac{\partial c}{\partial \tau}\Big/\frac{dc}{dz_F} \tag{44}$$

Finally, we obtain a set of equations that is a special case of eqs 1−6:

$$\frac{\partial z_F}{\partial \tau} = \frac{(1 - c(z_F))}{\partial c/\partial z_F} q \tag{45}$$

$$\frac{\partial q}{\partial x} = -(1 - c(z_F) + \sigma f(z_F)) q \tag{46}$$

$$\frac{\partial q_p}{\partial x} = -\sigma_E f_p(z_F) q_p \tag{47}$$

$$q(x = 0, t) = 1 \tag{48}$$

$$q_p(x = 0, t) = 1 \tag{49}$$

$$z_F(x, t = 0) = z_{F0} \tag{50}$$

Here, $x = \sigma_A A_0 X$. In the case of Model II, $z_{F0} = 0$. A comparison of eqs 45−50 with eqs 1−6 shows that there is a correspondence,

$$s \to z_F;$$

$$\Psi(s) \to \frac{1 - c(z_F)}{\partial c/\partial z_F};$$

$$\alpha(s) \to 1 - c(z_F) + \sigma^* f(z_F);$$

$$\alpha_p(s) \to \sigma^{**} f_p(z_F);$$

$$s_{init} = z_{F0} \tag{51}$$

Thus, we can write an expression for the absorbance at the probing wavelength (see 8)):

$$D_p(z_F^0) = \int_{z_F^l(z_F^0)}^{z_F^0} \frac{\frac{\sigma^{**}}{\sigma^*} f_p(z_F)\frac{dc(z_F)}{dz_F} dz_F}{(1 - c(z_F))\left(\frac{c(z_F) - c_{init}}{\sigma^*} + \int_{z_{F0}}^{z_F} \frac{f(z_F')}{1 - c(z_F')}\frac{dc(z_F')}{dz_F'} dz_F'\right)} \tag{52}$$

Here, z_F^0 is the value of z_F at $x = 0$, z_F^l is the value of z_F at $x = l = L/(\sigma_A A_0)$, and we used the apparent relation $\int_{z_{F0}}^{z_F} (dc(z_F')/dz_F') dz_F' = c\left(z_F\right) - c_{init}$.

The analog of eq 11 reads

$$\frac{dz_F}{dx} = -\frac{1}{\frac{dc}{dz_F}}(1 - c(z_F))\left(c(z_F) - c_{init} + \sigma^* \int_{z_{F0}}^{z_F} \frac{f(z_F')}{1 - c(z_F')}\frac{dc(z_F')}{dz_F'} dz_F'\right) \tag{53}$$

Solving the ordinary differential eq 53 with the boundary condition $z_F(x = 0) = z_F^0$ taken at $x = l$ gives the function $z_F^l(z_F^0)$ needed to calculate eq 52.

Relations 52 and 53 show that the required absorbance is an explicit function of z_F^0, which is the position in the size space of the leading front of the nanoparticle size distribution located on the irradiated surface of the sample, i.e., at the coordinate point $x = 0$. Using eq 32 at the point $x = 0$ (specifying $z_F = z_F^0$), we obtain the dependence of exposure on z_F^0:

$$E^0_{exp}(z_F^0) = \frac{1}{\beta} \ln\left(\frac{1 - c_{init}}{1 - c(z_F^0)}\right) \tag{54}$$

Fixing z_F^0, we find the value of $D_p(z_F^0)$ from eqs 52 and (53) and then the value of $E^0_{exp}(z_F^0)$ from eq 54. Excluding z_F^0 yields the dependence $D_p(E^0_{exp})$ that is measured in the experiment.

3.2. Fitting the Experimental Curves Obtained in 20.

Below we fit the experimental data by Model I and Model II.

The experimental data, namely, the absorbance of the films at the wavelength of the probing beam as a function of the UV exposure, are obtained in ref 20 at three different thermostat temperatures, 90, 100, and 110 °C.

https://doi.org/10.1021/acsomega.4c05121
ACS Omega 2024, 9, 36648−36658

The first feature of the experimental data is that the induced absorbance depends on the irradiation exposure. The data points taken at the same exposure and different UV intensities coincide with each other. This was taken into account in the development of the models described above.

The second feature of the experimental data is that the increase in absorbance at the probing wavelength in initially transparent samples starts after some delay in exposure E_{exp}^{**}. This is due to the fact that nanoparticles need some time to grow to the size at which they start to absorb light at the probing wavelength.

This feature is true both for Model I and Model II since (see eqs 39 and 52)

$$f_p(z) = 0 \text{ if } z < z^{**} \tag{55}$$

For Model I (see ref 29),

$$f_p(z_F) = g_0 F(z^{**}, z_F) \text{ if } z_R < z^{**} \tag{56}$$

$$f_p(z_F) = g_0 F(z_R, z_F) \text{ if } z_R \geq z^{**} \tag{57}$$

Correspondingly,

$$f(z_F) = g_0 F(z^{*}, z_F) \text{ if } z_R < z^{*} \tag{58}$$

$$f(z_F) = g_0 F(z_R, z_F) \text{ if } z_R \geq z^{*} \tag{59}$$

Here, the function F is determined in eq 28; $c(z_F)$ for Model I is determined in eq 30. It follows from eq 30 that

$$\frac{dc(z_F)}{dz_F} = \frac{g_0}{1 + z_F^{1/3}}\left((z_F - z_R) + 2\left(\frac{1}{z_F^{2/3}} - \frac{1}{z_R^{2/3}}\right)\right) \tag{60}$$

The function $z_R(z_F)$ is determined either by relation 26 or as a solution of the ordinary differential equation following from relation 26:

$$\frac{dz_R}{dz_F} = \frac{1 + z_R^{1/3}}{1 + z_F^{1/3}} \tag{61}$$

with condition $z_R(z_{F0}) = z_{R0}$.

In the experimental conditions $\sigma = 12.5$, $\sigma^{**} = 10.5$, and $l = 0.42$. We fix $z_{R0} = 70$.

Fitting parameters for Model I are β, which is proportional to the quantum yield η_A of the precursor destruction (see eq 32), z_{F0} and c_{init}, which determine g_0 at given z_{R0} and z_{F0} (see formulas 29 and 30). It is understood that $z_{F0} < z^{**}$ since the film is initially transparent at the probing wavelength. It should be noted that z_{F0} and c_{init} should have the same values for each temperatures because they characterize the properties of the film that do not depend on the treatment conditions. The quantum yield and thereby the value of β are temperature dependent.

The best fit to the experimental data (discrete points with bars) is shown in Figure 2. It corresponds to the smallest standard deviation achieved at $z_{F0} = 306$ and $c_{init} \approx 0.15$ ($g_0 \approx 2.3 \times 10^{-5}$). At 90 °C, $\beta \approx 2.8 \times 10^{-4}$ cm^2/J ($\eta_A \approx 3.7 \times 10^{-4}$), $E_{exp}^{**} = 100$ J/cm^2; at 100 °C, $\beta \approx 3.7 \times 10^{-4}$ cm^2/J ($\eta_A \approx 4.9 \times 10^{-4}$), $E_{exp}^{**} = 77$ J/cm^2; at 110 °C, $\beta \approx 5 \times 10^{-4}$ cm^2/J ($\eta_A \approx 6.7 \times 10^{-4}$) $E_{exp}^{**} = 57$ J/cm^2.

Figure 3 shows the dependence of fitting curves on the value of parameter z_{F0}.

For Model II (see ref 29), $c(z_F)$ is addressed in eq 36,

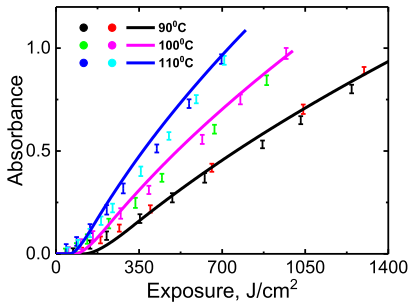

Figure 2. Comparison of experimental data (dots with bars) with theoretical $D_p(E_{exp})$ curves. Dark-blue and blue points correspond to data obtained at different light intensities (for detail, see ref 20) at the thermostat temperature 110 °C, the dark blue curve is the fitting one for this temperature, $z_{F0} = 306$ and $c_{init} \approx 0.15$ ($g_0 \approx 2.3 \times 10^{-5}$), $\beta \approx 5 \times 10^{-4}$ cm^2/J ($\eta_A \approx 6.7 \times 10^{-4}$), $E_{exp}^{**} = 57$ J/cm^2. Magenta and green points correspond to data obtained at different light intensities (for detail, see ref 20) at the thermostat temperature 100 °C, the magenta curve is the fitting one for this temperature, $z_{F0} = 306$ and $c_{init} \approx 0.15$ ($g_0 \approx 2.3 \times 10^{-5}$), $\beta \approx 3.7 \times 10^{-4}$ cm^2/J ($\eta_A \approx 4.9 \times 10^{-4}$), $E_{exp}^{**} = 77$ J/cm^2. Black and red points correspond to data obtained at different light intensities (for detail, see ref 20) at the thermostat temperature 90 °C, the black curve is the fitting one for this temperature. $z_{F0} = 306$ and $c_{init} \approx 0.15$ ($g_0 \approx 2.3 \times 10^{-5}$), $\beta \approx 2.8 \times 10^{-4}$ cm^2/J ($\eta_A \approx 3.7 \times 10^{-4}$), $E_{exp}^{**} = 100$ J/cm^2.

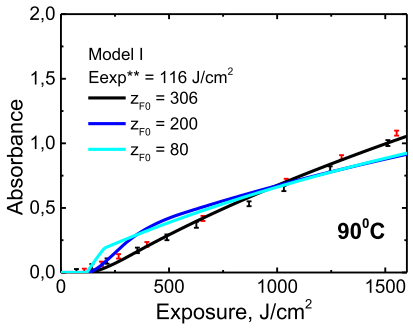

Figure 3. Effect of the value of parameter z_{F0} on the fitting curves. The black curve is the best fit: $z_{F0} = 306$, $c_{init} \approx 0.15$, and $g_0 \approx 2.3 \times 10^{-5}$ (see Figure 2). The dark blue curve corresponds to $z_{F0} = 200$, $c_{init} \approx 0.02$, and $g_0 \approx 6.9 \times 10^{-6}$ and the blue curve to $z_{F0} = 80$, $c_{init} \approx 6 \times 10^{-3}$, and $g_0 \approx 4.2 \times 10^{-5}$.

$$f(z_F) = \Theta(z_F - z^{*})\cdot c(z_F)\cdot\left(1 - \frac{j(\gamma, z^{*})}{j(\gamma, z_F)}\right) \tag{62}$$

$$f_p(z_F) = \Theta(z_F - z^{**})\cdot c(z_F)\cdot\left(1 - \frac{j(\gamma, z^{**})}{j(\gamma, z_F)}\right) \tag{63}$$

$$\frac{dc}{dz_F} = \frac{c(z_F)}{1 + z_F^{1/3}}\left(-\gamma + \frac{z_F\cdot\exp(\gamma\xi_F(z_F))}{j(\gamma, z_F)}\right) \tag{64}$$

Here, $\Theta(z)$ is a Heaviside function, and $j(\gamma,z)$ and $\xi(z)$ are addressed in eqs 37 and 18. The fitting parameters for Model II are β, parameter γ, and $\overline{B}_{00}/A_0$.

When simultaneously fitting the three sets of the data corresponding to different thermostat temperatures by the model II, we should keep the same value of the parameter $\overline{B}_{00}/A_0$ for all three curves. Parameters β and γ depend on the thermostat temperature.

Figure 4 shows the best fit to the experimental data. It corresponds to the smallest standard deviation achieved at $\overline{B}_{00}/$

https://doi.org/10.1021/acsomega.4c05121
ACS Omega 2024, 9, 36648−36658

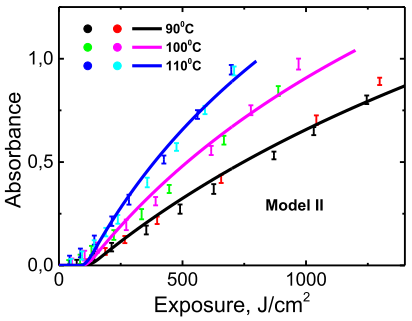

Figure 4. Comparison of experimental data (dots with bars) with theoretical $D_p(E_{exp})$ curves (Model II). Dark-blue and blue points correspond to data obtained at different light intensities (for detail, see ref 20) at the thermostat temperature 110 °C, the dark blue curve is the fitting one for this temperature, $\bar{B}_{00}/A_0 = 7.2 \times 10^{-3}$, $\gamma = 10^{-3}$, $\beta \approx 7 \times 10^{-4}$ cm^2/J, ($\eta_A \approx 9.3 \times 10^{-4}$), E_{exp}** = 88 J/cm^2. Magenta and green points correspond to data obtained at different light intensities (for detail, see ref 20) at the thermostat temperature 100 °C, the magenta curve is the fitting one for this temperature, $\bar{B}_{00}/A_0 = 7.2 \times 10^{-3}$, $\gamma = 7 \times 10^{-4}$, $\beta \approx 4.6 \times 10^{-4}$ cm^2/J ($\eta_A \approx 6.1 \times 10^{-4}$), E_{exp}** = 93 J/cm^2. Black and red points correspond to data obtained at different light intensities (for detail, see ref 20) at the thermostat temperature 90 °C, the black curve is the fitting one for this temperature. $\bar{B}_{00}/A_0 = 7.2 \times 10^{-3}$, $\gamma = 5 \times 10^{-4}$, $\beta \approx 3 \times 10^{-4}$ cm^2/J, ($\eta_A \approx 4 \times 10^{-4}$), E_{exp}** = 104 J/cm^2.

$A_0 = 7.2 \times 10^{-3}$. At 90 °C, $\gamma = 5 \times 10^{-4}$, $\beta \approx 3 \times 10^{-4}$ cm^2/J, ($\eta_A \approx 4 \times 10^{-4}$), E_{exp}** = 104 J/cm^2, at 100 °C, $\gamma = 7 \times 10^{-4}$, $\beta \approx 4.6 \times 10^{-4}$ cm^2/J ($\eta_A \approx 6.1 \times 10^{-4}$), E_{exp}** = 93 J/cm^2, at 110 °C, $\gamma = 10^{-3}$, $\beta \approx 7 \times 10^{-4}$ cm^2/J, ($\eta_A \approx 9.3 \times 10^{-4}$), E_{exp}** = 88 J/cm^2.

Figure 5 shows dependence of fitting curves on the value of parameter γ.

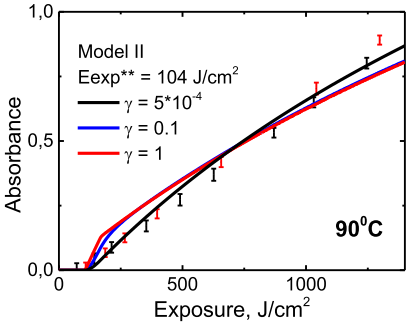

Figure 5. Effect of the value of parameter γ on the fitting curves. The black curve is the best fit: $\gamma = 5 \times 10^{-4}$, $\gamma\bar{B}_{00}/A_0 = 3.6 \times 10^{-7}$, $\beta \approx 3 \times 10^{-4}$ cm^2/J (see Figure 4). The dark blue curve corresponds to $\gamma = 0.1$, $\gamma\bar{B}_{00}/A_0 = 8.6 \times 10^{-6}$, $\beta \approx 2.2 \times 10^{-4}$ cm^2/J and the red curve to $\gamma = 1$, $\gamma\bar{B}_{00}/A_0 = 6.9 \times 10^{-5}$, $\beta \approx 2.2 \times 10^{-4}$ cm^2/J.

The results show that the best fit parameters in both cases of Models I and II correspond to broad size distributions (see Figures 4, 6, and 7).

3.3. Growth of Core−Shell Nanoparticles. Below we study the case where the initially existing nanoparticles considered in the previous chapters of this paper are of a different nature than the growing nanoparticles. Monomers deposited on such nanoparticles form shells, thus building core−shell nanoparticles. Such core nanoparticles are the growth centers of nanoparticles along with the existing centers of number density $\bar{B}_{00}$ considered above (see Figure 8).

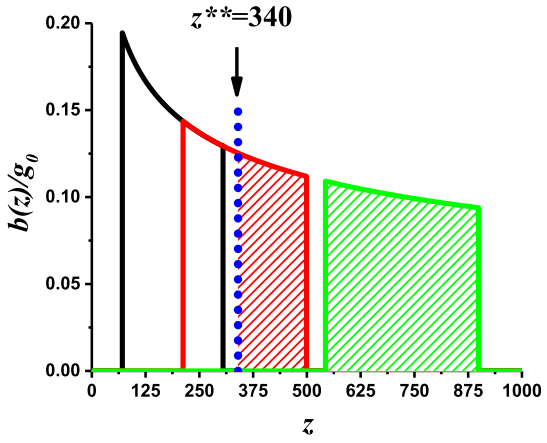

Figure 6. Normalized particle-size distributions calculated within Model I, $z_{F0} = 306$. Different colors correspond to different values of UV exposure; z** denotes the minimum size of a particle that absorbs light at the probing wavelength. The black curve corresponds to the early stage of the process where the composite material remains transparent. The onset of the absorption occurs when the particle size distribution reaches z** (red curve). The green curve corresponds to the stage where the entire particle size distribution contributes to the absorption of the composite.

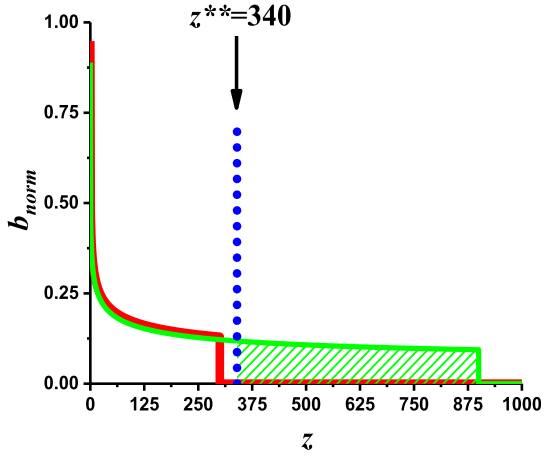

Figure 7. Normalized particle-size distributions calculated within Model II, $\gamma = 0.001$. Different colors correspond to different values of UV exposure; z** denotes the minimum size of a particle that absorbs light at the probing wavelength. The red curve corresponds to a transparent sample at early stages of the process. The green curve corresponds to later stages where the sample absorbs the probing light.

The diffusion-controlled shell growth suggests that the growth constant is determined by the radius of the nanoparticle. This means that if the initial radius of the core nanoparticle is R, it corresponds to the value of the variable

$$z = \frac{4\pi R^3}{3V_1} \tag{65}$$

Here V_1 is the volume of the native monomer, e.g., for CdS, $V_1 = 4.83 \times 10^{-23}$ cm^3. The initial distribution of core nanoparticles is addressed in eq 21 in variables (g,ξ) and the evolution of this distribution in physical variables (b, z), in eq 25. The distribution of native nanoparticles is considered in eq 33. Importantly, these distributions in variables (g, ξ) are parts of the same profile. This means that when profile (21) is

https://doi.org/10.1021/acsomega.4c05121
ACS Omega 2024, 9, 36648−36658

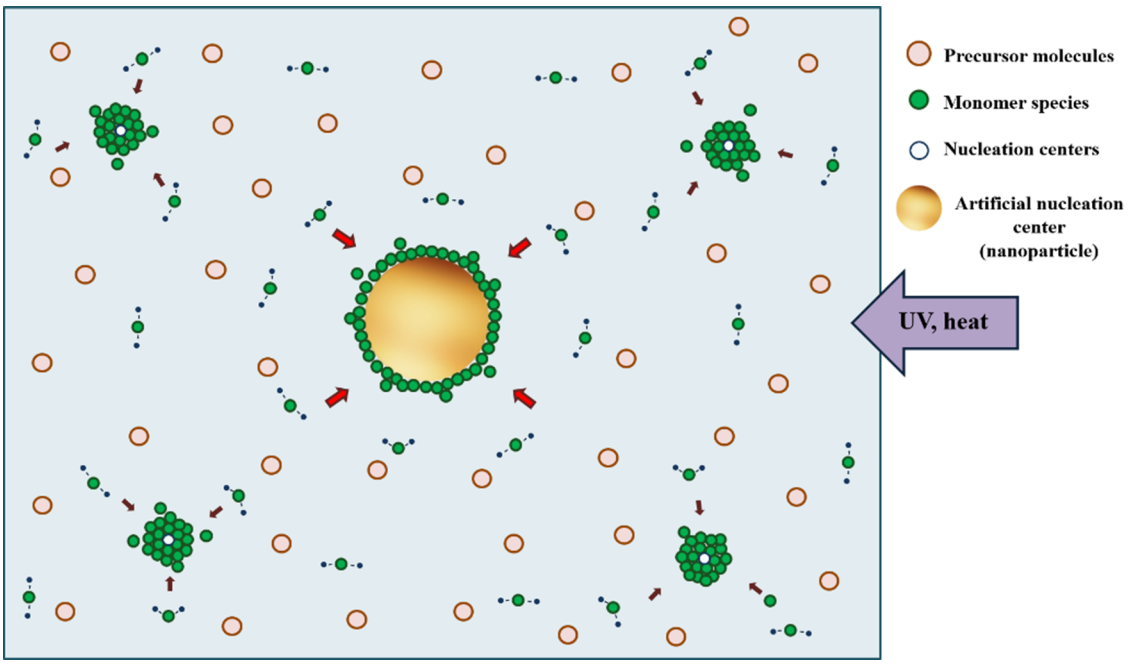

Figure 8. Monomers formed by the decomposition of precursor compounds come either to existing nanoparticles of a different nature that build shells or to crystallization centers that build native nanoparticles.

shifted by $\delta\xi$, the profile (eqs 33 and 34) is also shifted by the same value of $\delta\xi$.

Thus, the relevant parameter in this problem is $\delta\xi$, a shift of the profile consisting of two parts, the first of which relates to the growth of core−shell nanoparticles and the second, to the growth of native nanoparticles.

Given $\delta\xi$, we can calculate c_1, the number density of monomers that make up the shells,

$$c_1(\delta\xi) = c_{\text{core}}\left(\frac{F(z_R(\xi_{R0} + \delta\xi), z_F(\xi_{F0} + \delta\xi))}{F(z_{R0}, z_{F0})} - 1\right) \quad (66)$$

and c_2, the number density of monomers in native nanoparticles growing at $\bar{B}_{00}$ centers.

$$c_2(\delta\xi) = \gamma\frac{\bar{B}_{00}}{A_0}\exp(-\gamma\xi(z_F(\delta\xi))j(\gamma, z_F(\delta\xi)) \quad (67)$$

In eq 66 (see eq 29),

$$c_{\text{core}} = g_0 F(z_{R0}, z_{F0}) \quad (68)$$

is proportional to the number density of "alien" monomers constituting the core nanoparticles.

The function $z(\xi)$ is determined in implicit form by eq 18.

Knowing c_1 and c_2, one can calculate the number density of monomers within the nanoparticles of two species,

$$c(\delta\xi) = c_1(\delta\xi) + c_2(\delta\xi) \quad (69)$$

Excluding the variable $\delta\xi$, we obtain the dependences $c_1(c)$ and $c_2(c)$ in parametric form (see Figure 9).

Taking the values of the maximal and minimum core radii of the nanoparticles, we can calculate z_{R0} and z_{F0} using eq 65. Using eq 18, we can find ξ_{R0} and ξ_{F0}. Calculating the values of $z_R(\xi + \delta\xi)$ and $z_F(\xi + \delta\xi)$, we obtain $z_R(\xi + \delta\xi) - z_{R0}$ and $z_F(\xi + \delta\xi) - z_{F0}$. Knowing the monomer volume (see eq 65), we can obtain the shell volume for the maximum and minimum radii of the core−shell nanoparticles, and using simple geometric formulas, we find the corresponding shell thicknesses d_F and d_R as functions of $\delta\xi$ and thus as functions of the variable c (see eqs 66−69). The corresponding dependences are shown in Figure 10.

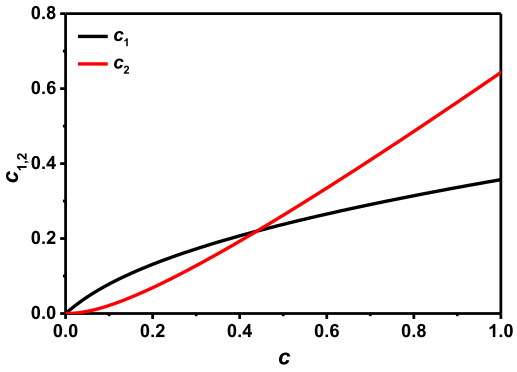

Figure 9. Evolution of the number density of monomers constituting the shell structures (black color) and native nanoparticles (red color) for $c_{\text{core}} = 0.5$, $\bar{B}_{00}/A_0 \approx 7.2 \cdot 10^{-3}$and $\gamma = 5 \times 10^{-4}$. The core nanoparticle radii lie in the range $R_{R0} < R < R_{F0}$; $R_{R0} = 3$ nm and $R_{F0} = 5$ nm.

An important parameter is c_{core}, which determines the number of core nanoparticles. The dependence of the fraction of monomers within the shells and the shell thickness on this parameter is shown in Figures 11 and 12.

It is seen that a significant number of monomers enter the shell at a relatively high value of the parameter c_{core}. With increasing c_{core}, the shell thickness decreases due to an increase in the number of core nanoparticles.

It is interesting to find out the dependence of the shell growth process on the parameter γ, the efficiency of crystallization centers.

If we fix the parameter $\bar{B}_{00}/A_0$, then the smaller γ, the more efficient the shell growth. However, if we fix the value of the

https://doi.org/10.1021/acsomega.4c05121
ACS Omega 2024, 9, 36648−36658

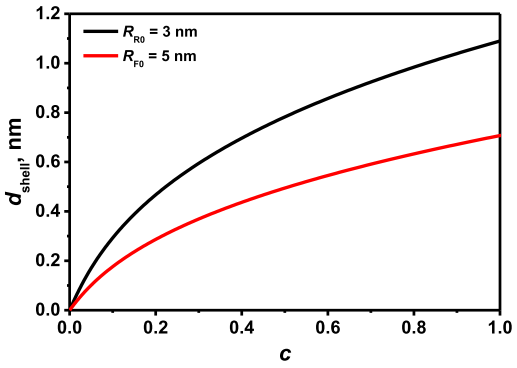

Figure 10. Evolution of the shell thickness for core nanoparticles with radii of 3 and 5 nm; $\overline{B}_{00}/A_0 \approx 7.2 \times 10^{-3}$, $\gamma = 5 \times 10^{-4}$ and $c_{core} = 0.5$.

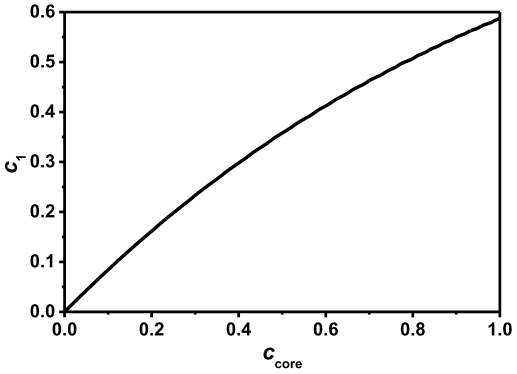

Figure 11. Dependence of the fraction of monomer constituting the shells on the value of the parameter c_{core} at $c = 1$; $\overline{B}_{00}/A_0 \approx 7.2 \times 10^{-3}$, and $\gamma = 5 \times 10^{-4}$, $R_{R0} = 3$ nm, and $R_{F0} = 5$ nm.

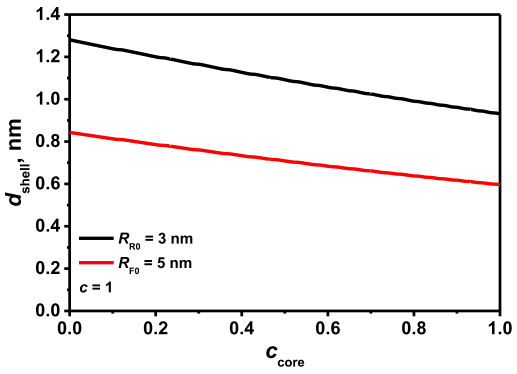

Figure 12. Shell thickness as a function of c_{core} at $c = 1$; $\overline{B}_{00}/A_0 \approx 7.2 \times 10^{-3}$, and $\gamma = 5 \times 10^{-4}$, $R_{R0} = 3$ nm, and $R_{F0} = 5$ nm.

parameter $\gamma\overline{B}_{00}/A_0$, the result is opposite. (See Figures 13 and 14).

4. CONCLUSIONS

Experimental data on the nucleation and growth of CdS nanoparticles in a polymer film initiated by photochemical decomposition of a well-soluble precursor compound show the dependence of the process parameters on light exposure. Theoretical models of this phenomenon were constructed in a previous publication.[29] In the present work, these models are applied to find the exposure dependence of the absorbance of optically thick films. In addition to the above models describing the exposure-dependent growth of nanoparticles, we also use the approach considered in ref 37. The important

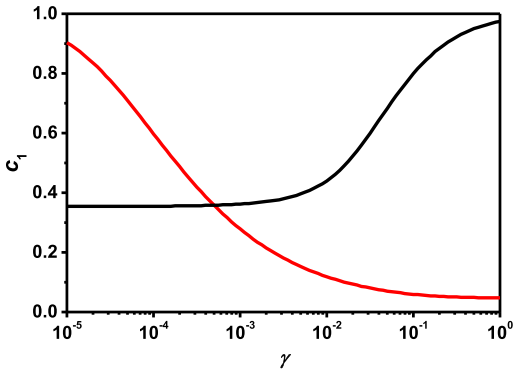

Figure 13. Dependence of the shell growth efficiency, the fraction of monomers constituting the shells, on the parameter γ at a fixed value of $\overline{B}_{00}/A_0 = 7.2 \times 10^{-3}$ (red curve) and a fixed value of $\gamma\overline{B}_{00}/A_0 = 3.6 \times 10^{-6}$ (black curve); $c_{core} = 0.5$ and $c = 1$.

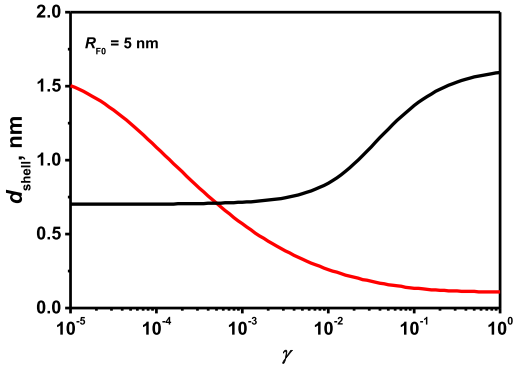

Figure 14. Dependence of the maximum shell thickness for core nanoparticles with $R = 5$ nm, on the parameter γ at a fixed value of $\overline{B}_{00}/A_0 = 7.2 \times 10^{-3}$ (red curve) and a fixed value of $\gamma\overline{B}_{00}/A_0 = 3.6 \times 10^{-6}$ (black curve); $c_{core} = 0.5$ and $c = 1$.

point here is the choice of an appropriate single variable that fully characterizes the growth process. This permits one to represent the absorption coefficient as an explicit function of this parameter. In the considered case, such a variable is z_F, the number of CdS units in the largest nanoparticle in the continuous approximation. The use of the analytical technique makes it possible to identify the main parameters involved and determine their values by fitting experimental curves. The exposure-dependent absorbance growth suggests a heterogeneous nucleation process. This means that some kind of nucleation centers is initially present in the material. We consider two types of these centers. Centers of the first type are nanoparticles that spontaneously appeared in the material before irradiation. In this case, the fitting parameters are the quantum yield of precursor destruction η_A, the initial value of the variable z_F, that is, z_{F0} (the size of the smallest nanoparticle is fixed by the condition of their immobility), and the percentage of precursor molecules spontaneously decomposed during sample preparation. The fitting yields $z_{F0} = 306$ and 15% of the precursor compound initially decomposed. The quantum yield of the precursor decomposition depends on the thermostat temperature, $\eta_A \approx 3.7 \times 10^{-4}$ at 90 °C, $\eta_A \approx 4.9 \times 10^{-4}$ at 100 °C, and $\eta_A \approx 6.7 \times 10^{-4}$ at 110 °C.

Nucleation centers of the second type are crystallization centers related to polymer chains. In addition to the quantum yield of precursor destruction, the fitting parameters here are the parameter γ, which is relative nucleation rate with respect

https://doi.org/10.1021/acsomega.4c05121
ACS Omega 2024, 9, 36648−36658

to the diffusion-controlled limit, and the number density of nucleation centers relative to the number density of precursor molecules, $\bar{B}_{00}/A_0$. The fitting yields $\bar{B}_{00}/A_0 = 7.2 \times 10^{-3}$. The value of parameter γ and the quantum yield of the precursor decomposition depend on the thermostat temperature, $\gamma = 5 \times 10^{-4}$, $\eta_A \approx 4 \times 10^{-4}$ at 90 °C, $\gamma = 7 \times 10^{-4}$, $\eta_A \approx 6.1 \times 10^{-4}$ at 100 °C, and $\gamma = 10^{-3}$, $\eta_A \approx 9.3 \times 10^{-4}$ at 110 °C.

The fitting parameters for both models indicate a wide size distribution of nanoparticles.

If the nucleation centers of the first type are nanoparticles of a different nature, for example, gold nanoparticles, the attachment of monomers to such nanoparticles leads to the growth of core−shell structures. Competition arises between core−shell growth and the growth of pure native nanoparticles in nucleation centers of the second type. This problem for realistic values of the parameters found in the first part of the paper is considered in the second part. The thickness of growing shells and the fraction of monomers participating in the shell growth process are estimated.

It is shown that the effect depends significantly on the number of core nanoparticles and their size. For realistic parameter values, the number density of monomers constituting the core nanoparticles, comparable to the density of precursor monomers for native monomers, is required for an efficient core growth process. The efficiency of the centers of the second type is characterized by the parameter γ. It is shown that at a fixed density of nucleation centers of the second type, an increase in the parameter γ will lead to a significant decrease in the shell growth process, while at a fixed value of the parameter $\gamma\bar{B}_{00}/A_0$, an increase in the parameter γ leads to the opposite result.

AUTHOR INFORMATION

Corresponding Author

Nikita Bityurin − *Institute of Applied Physics of the Russian Academy of Sciences, 603950 Nizhny Novgorod, Russia;* orcid.org/0000-0001-5959-7161; Email: bit@appl.sci-nnov.ru

Authors

Natalia Sapogova − *Institute of Applied Physics of the Russian Academy of Sciences, 603950 Nizhny Novgorod, Russia*

Andrey Kudryashov − *Institute of Applied Physics of the Russian Academy of Sciences, 603950 Nizhny Novgorod, Russia*

Alexander Pikulin − *Institute of Applied Physics of the Russian Academy of Sciences, 603950 Nizhny Novgorod, Russia;* orcid.org/0000-0001-9876-1147

Complete contact information is available at: https://pubs.acs.org/10.1021/acsomega.4c05121

Notes

The authors declare no competing financial interest.

ACKNOWLEDGMENTS

The authors thank the Center of Excellence "Center of Photonics" funded by the Ministry of Science and Higher Education of the Russian Federation, contract no. 075-15-2022-316 for financial support.

REFERENCES

(1) Bityurin, N.; Alexandrov, A.; Afanasiev, A.; Agareva, N.; Pikulin, A.; Sapogova, N.; Soustov, L.; Salomatina, E.; Gorshkova, E.; Tsverova, N.; Smirnova, L. Photoinduced Nanocomposites—Creation, Modification, Linear and Nonlinear Optical Properties. *Appl. Phys. A: Mater. Sci. Process.* **2013**, *112*, 135−138.

(2) Persano, L.; Camposeo, A.; Laera, A. M.; Benedetto, F. D.; Resta, V.; Tapfer, L.; Pisignano, D. In situ thermal, photon, and electron-beam synthesis of polymer nanocomposites. In *Synthesis Techniques for Polymer Nanocomposites*; Mittal, V., Ed.; Wiley-VCH: Weinheim, Germany, 2014; pp 289−314.

(3) Antolini, F.; Orazi, L. Quantum Dots Synthesis Through Direct Laser Patterning: A Review. *Front. Chem.* **2019**, *7*, 252.

(4) Stellacci, F.; Bauer, C. A.; Meyer-Friedrichsen, T.; Wenseleers, W.; Alain, V.; Kuebler, S. M.; Pond, S. J. K.; Zhang, Y.; Marder, S. R.; Perry, J. W. Laser and Electron-Beam Induced Growth of Nanoparticles for 2D and 3D Metal Patterning. *Adv. Mater.* **2002**, *14* (3), 194−198.

(5) Alexandrov, A.; Smirnova, L.; Yakimovich, N.; Sapogova, N.; Soustov, L.; Kirsanov, A.; Bityurin, N. UV-Initiated Growth of Gold Nanoparticles in PMMA Matrix. *Appl. Surf. Sci.* **2005**, *248* (1−4), 181−184.

(6) Antolini, F.; Ghezelbash, A.; Esposito, C.; Trave, E.; Tapfer, L.; Korgel, B. A. Laser-Induced Nanocomposite Formation for Printed Nanoelectronics. *Mater. Lett.* **2006**, *60* (8), 1095−1098.

(7) Athanassiou, A.; Cingolani, R.; Tsiranidou, E.; Fotakis, C.; Laera, A. M.; Piscopiello, E.; Tapfer, L. Photon-Induced Formation of CdS Nanocrystals in Selected Areas of Polymer Matrices. *Appl. Phys. Lett.* **2007**, *91*, 153108.

(8) Fragouli, D.; Resta, V.; Pompa, P. P.; Laera, A. M.; Caputo, G.; Tapfer, L.; Cingolani, R.; Athanassiou, A. Patterned Structures of in Situ Size Controlled CdS Nanocrystals in a Polymer Matrix under UV Irradiation. *Nanotechnology* **2009**, *20*, No. 155302.

(9) Alsawafta, M.; Badilescu, S.; Paneri, A.; Truong, V.-V.; Packirisamy, M. Gold-Poly(Methyl Methacrylate) Nanocomposite Films for Plasmonic Biosensing Applications. *Polymers* **2011**, *3* (4), 1833−1848.

(10) Fragouli, D.; Pompa, P. P.; Kalayva, M.; Caputo, G.; Tapfer, L.; Cingolani, R.; Athanassiou, A. The effect of irradiation wavelength on the quality of CdS nanocrystals formed directly into PMMA matrix. *J. Phys. Chem. C* **2010**, *114* (33), 13985−13990.

(11) Yilmaz, E.; Suzer, S. Au nanoparticles in PMMA matrix: In situ synthesis and the effect of Au nanoparticles on PMMA conductivity. *Appl. Surf. Sci.* **2010**, *256* (22), 6630−6633.

(12) Resta, V.; Laera, A. M.; Piscopiello, E.; Schioppa, M.; Tapfer, L. Highly efficient precursors for direct synthesis of tailored CdS nanocrystals in organic polymers. *J. Phys. Chem. C* **2010**, *114* (41), 17311−17317.

(13) Fragouli, D.; Laera, A. M.; Caputo, G.; Resta, V.; Pompa, P. P.; Tapfer, L.; Cingolani, R.; Athanassiou, A. The effect of polymer matrices in the in-situ CdS formation under UV irradiation of precursor-polymer films. *J. Nanosci. Nanotechnol.* **2010**, *10* (2), 1267−1272.

(14) Camposeo, A.; Polo, M.; Neves, A. A. R.; Fragouli, D.; Persano, L.; Molle, S.; Laera, A. M.; Piscopiello, E.; Resta, V.; Athanassiou, A.; Cingolani, R.; Tapfer, L.; Pisignano, D. Multi-photon in situ synthesis and patterning of polymer-embedded nanocrystals. *J. Mater. Chem.* **2012**, *22* (19), 9787.

(15) Resta, V.; Laera, A. M.; Camposeo, A.; Piscopiello, E.; Persano, L.; Pisignano, D.; Tapfer, L. Spatially confined CdS NCs in-situ synthesis through laser irradiation of suitable unimolecular precursor-doped polymer. *J. Phys. Chem. C* **2012**, *116* (47), 25119−25125.

(16) Onwudiwe, D. C.; Krüger, T. P. J.; Strydom, C. A. Laser assisted solid state reaction for the synthesis of ZnS and CdS nanoparticles from metal xanthate. *Mater. Lett.* **2014**, *116*, 154−159.

(17) Limosani, F.; Carcione, R.; Antolini, F. Formation of CdSe quantum dots from single source precursor obtained by thermal and laser treatment. *J. Vac. Sci. Technol. B* **2020**, *38* (1), No. 012802.

(18) Agareva, N.; Smirnov, A. A.; Afanasiev, A.; Sologubov, S.; Markin, A.; Salomatina, E.; Smirnova, L.; Bityurin, N. Properties of cadmium-(*bis*)dodecylthiolate and polymeric composites based on it. *Materials* **2015**, *8* (12), 8691−8700.

https://doi.org/10.1021/acsomega.4c05121
ACS Omega 2024, 9, 36648−36658

(19) Bansal, A. K.; Sajjad, M. T.; Antolini, F.; Stroea, L.; Gečys, P.; Raciukaitis, G.; André, P.; Hirzer, A.; Schmidt, V.; Ortolani, L.; Toffanin, S.; Allard, S.; Scherfh, U.; Samuel, I. D. W. In situ formation and photo patterning of emissive quantum dots in small organic molecules. *Nanoscale* **2015**, *7*, 11163.
(20) Smirnov, A. A.; Afanasiev, A.; Gusev, S.; Tatarskiy, D.; Ermolaev, N.; Bityurin, N. Exposure dependence of the UV initiated optical absorption increase in polymer films with a soluble CdS precursor and its relation to the photoinduced nanoparticle growth. *Opt. Mater. Express* **2018**, *8* (6), 1603−1612.
(21) Antolini, F.; Orazi, L. Solid state synthesis of CdS quantum dots through laser direct writing. *AIP Conf. Proc.* **2019**, *2145* (1), No. 020016.
(22) Agareva, N.; Smirnov, A. A.; Salomatina, E.; Smirnova, L.; Afanasiev, A.; Gusev, S.; Tatarskiy, D.; Bityurin, N. Photoinduced nanocomposites based on soluble precursor of CdS nanoparticles in polymethyl methacrylate matrix obtained by bulk radical polymerization. *Polym. Bull.* **2021**, *78*, 1941−1953.
(23) Bityurin, N.; Ermolaev, N.; Smirnov, A. A.; Afanasiev, A.; Agareva, N.; Koryukina, T.; Bredikhin, V.; Kamenskiy, V.; Pikulin, A.; Sapogova, N. Plasmonic, excitonic and exciton-plasmonic photo-induced nanocomposites. *Appl. Phys. A: Mater. Sci. Process.* **2016**, *122*, 193.
(24) Bityurin, N.; Kudryashov, A. Diffusion-assisted ultrashort laser pulse induced photothermal growth of core-shell nanoparticles in polymer matrix. *Opt. Express* **2021**, *29* (23), 37376−37398.
(25) Smirnov, A. A.; Elagin, V.; Afanasiev, A.; Pikulin, A.; Bityurin, N. Luminescent patterns recorded by laser irradiation of a PMMA matrix with a soluble CdS precursor. *Opt. Mater. Express* **2020**, *10* (9), 2114−2125.
(26) Ramasamy, K.; Malik, M. A.; Helliwell, M.; Raftery, J.; O'Brien, P. Thio- and dithio-biuret precursors for zinc sulfide, cadmium sulfide, and zinc cadmium sulfide thin films. *Chem. Mater.* **2011**, *23* (6), 1471−1481.
(27) Smirnov, A. A.; Afanasiev, A.; Ermolaev, N.; Bityurin, N. LED induced green luminescence in visually transparent PMMA films with CdS precursor. *Opt. Mater. Express* **2016**, *6* (1), 290−295.
(28) Pikulin, A.; Bityurin, N. Homogeneous Model for the Nanoparticle Growth in Polymer Matrices. *J. Phys. Chem. C* **2020**, *124* (29), 16136−16142.
(29) Bityurin, N.; Sapogova, N.; Pikulin, A. Heterogeneous model for precursor-mediated nanoparticle growth in polymer film. *J. Phys. Chem. C* **2023**, *127* (37), 18442−18453.
(30) Kuznetsov, A.; Kameneva, O.; Alexandrov, A.; Bityurin, N.; Marteau, Ph.; Chhor, K.; Sanchez, C.; Kanaev, A. Light-induced charge separation and storage in titanium oxide gels. *Phys. Rev. E* **2005**, *71* (2), No. 021403.
(31) Bityurin, N.; Kuznetsov, A. I.; Kanaev, A. Kinetics of UV induced darkening of titanium − oxide gels. *Appl. Surf. Sci.* **2005**, *248* (1−4), 86−90.
(32) Kuznetsov, A. I.; Kameneva, O.; Bityurin, N.; Rozes, L.; Sanchez, C.; Kanaev, A. Laser-induced photopatterning of organic-inorganic TiO_2 based hybrid materials with tunable interfacial electron transfer. *Phys. Chem. Chem. Phys.* **2009**, *11* (8), 1248−1257.
(33) Chelnokov, E.; Soustov, L.; Sapogova, N.; Ostrovsky, M.; Bityurin, N. Nonreciprocal XeCl laser-induced aggregation of beta-crystallins in water solution. *Opt. Express* **2008**, *16* (23), 18798−18803.
(34) Smirnov, A. A.; Kudryashov, A.; Agareva, N.; Afanasiev, A.; Gusev, S.; Tatarskiy, D.; Bityurin, N. In-situ monitoring of the evolution of the optical properties for UV LED irradiated polymer-based photo-induced nanocomposites. *Appl. Surf. Sci.* **2019**, *486*, 376−382.
(35) Bityurin, N. UV etching accompanied by modifications. Surface etching. *Appl. Surf. Sci.* **1999**, *138−139*, 354−358.
(36) Bityurin, N.; Luk'yanchuk, B. S.; Hong, M. H.; Chong, T. C. Models for laser ablation of polymers. *Chem. Rev.* **2003**, *103* (2), 519−552.
(37) Bityurin, N.; Smirnov, A. A. Model for UV induced growth of semiconductor nanoparticles in polymer films. *Appl. Surf. Sci.* **2019**, *487*, 678−691.
(38) Reiss, P.; Protière, M.; Li, L. Core/Shell Semiconductor Nanocrystals. *Small* **2009**, *5* (2), 154−168.
(39) Ghosh Chaudhuri, R.; Paria, S. Core/Shell Nanoparticles: Classes, Properties, Synthesis Mechanisms, Characterization, and Applications. *Chem. Rev.* **2012**, *112* (4), 2373−2433.
(40) Kagan, C. R.; Bassett, L. C.; Murray, C. B.; Thompson, S. M. Colloidal Quantum Dots as Platforms for Quantum Information Science. *Chem. Rev.* **2021**, *121* (5), 3186−3233.
(41) Jiang, R.; Li, B.; Fang, C.; Wang, J. Metal/Semiconductor Hybrid Nanostructures for Plasmon-Enhanced Applications. *Adv. Mater.* **2014**, *26* (31), 5274−5309.
(42) Zhang, J.; Tang, Y.; Lee, K.; Ouyang, M. Nonepitaxial Growth of Hybrid Core-Shell Nanostructures with Large Lattice Mismatches. *Science* **2010**, *327* (5973), 1634−1638.
(43) Huang, L.; Zheng, J.; Huang, L.; Liu, J.; Ji, M.; Yao, Y.; Xu, M.; Liu, J.; Zhang, J.; Li, Y. Controlled Synthesis and Flexible Self-Assembly of Monodisperse Au@Semiconductor Core/Shell Hetero-Nanocrystals into Diverse Superstructures. *Chem. Mater.* **2017**, *29* (5), 2355−2363.
(44) Wang, L.; Li, R.; Liu, J.; Han, J.; Huang, M. Synthesis of Au@CdS Core−Shell Nanoparticles and Their Photocatalytic Capacity Researched by SERS. *J. Mater. Sci.* **2017**, *52*, 1847−1855.
(45) Stockman, M. I. Brief History of Spaser from Conception to the Future. *Adv. Photon.* **2020**, *2* (5), No. 054002.

https://doi.org/10.1021/acsomega.4c05121
ACS Omega 2024, 9, 36648−36658